One-step flame synthesis of SnO_2/TiO_2 composite nanoparticles for photocatalytic applications

Kranthi K. Akurati,[1] Andri Vital,[1,†] Roland Hany,[1] Bastian Bommer,[1] Thomas Graule,[1] and Markus Winterer[2]

[1] *Empa Materials Testing and Research, Laboratory for High Performance Ceramics, CH-8600 Duebendorf, Switzerland*

[2] *University of Duisburg-Essen, Institute of Combustion and Gas Dynamics, Nanoparticle Process Technology, Lotharstr. 1, D-47057 Duisburg, Germany*

ABSTRACT. SnO_2/TiO_2 composite nanoparticles have been synthesized in a single-step by feeding evaporated precursor mixtures into an atmospheric pressure diffusion flame. Particles with controlled Ti : Sn ratios were produced at various flow rates of oxygen, and the resulting powders were characterized by BET surface area analysis, XRD, TEM, EDAX and UV-Vis spectroscopy. For the lowest concentration (3.4 mol%) of SnO_2 employed in this study anatase phase of TiO_2 is stabilized, while segregation of SnO_2 is seen at medium (6.9 to 12.4 mol%) and high concentrations (20.3 mol%). Though the equilibrium phase diagram predicts complete solubility of one oxide in another at all compositions, segregation of SnO_2 phase is observed which is explained by the usage of diffusion flame in the present study. The particle formation mechanism of SnO_2/TiO_2 composites is proposed basing on the single component aerosol formation. Photocatalytic activity of the composite particles is tested for the degradation of methylene blue and is compared with pure TiO_2 synthesized under similar conditions. Improved photocatalytic activity of the composite particles is attributed to the stabilized anatase phase and better charge separation due to the coupling of TiO_2 and SnO_2 within the composite nanoparticles.

1. INTRODUCTION

Interest in the study of TiO_2 as photocatalyst was triggered in 1972 by Fujishima and Honda, who first demonstrated its use for photo-oxidation of water [1]. Since then considerable research has been done from both fundamental and an applied perspective. Although a few studies have explored the photocatalytic activity of other semiconductors such as SnO_2 [2], ZnO [3], Nb_2O_5 [4], CeO_2 [5], $SrTiO_3$ [6], CdS, HgS, ZnS, CdSe, Ga_2S_3 [7] and CdTe [8], the preponderance of work has focused on TiO_2 due to its suitable thermodynamic positions of valence and conduction band edges for redox reactions, long term stability, low cost, non-toxicity, resistance to photo and chemical corrosion [9, 10]. In spite of its numerous advantages, widespread commercial application of TiO_2 is hindered because of low efficiency [11]. Quantum efficiency of the photocatalytic process, that is, the rate at which the desired oxidation products are formed divided by the absorbed photon flux, is determined by the competition for carriers between the reactions of oxidation and reduction on one hand and processes of recombination on the other hand. Riegel and co-workers [12] studied the variations in rate constants related to recombination and/or oxidation which varies the steady-state photocatalytic efficiency and concluded, based on a simple kinetic model, that the observed variability arises specially from variations in the rate constant for recombination. So suppression of recombination of the photogenerated charge carriers is essential for improving the efficiency. Several researches proved that the recombination is prevented by semiconductor-metal composites or by employing two different semiconductors. Modification of TiO_2 by noble metal deposition i.e. Au [13–15], Ag [16], Pt [17] increases photocatalytic efficiency. When the deposited metal particle interacts with the photoexcited TiO_2, the two particles undergo charge equilibration. The shift in the Fermi level towards the conduction band energy enhances the catalytic efficiency of the composite system. However, the associated processes and reagents are expensive which makes it difficult to scale-up the process.

Efficiency can also be increased by coupling two semiconductors which have suitable conduction and valence band potentials. In the past years, a number of studies related to TiO_2 coupled with other semiconductors like SnO_2 [18, 19], WO_3 [20, 21], Fe_2O_3 [22, 23], ZnO [24], CdS [25], Cd_3P_2 [26] were performed. Among them, coupling TiO_2 with SnO_2 attracts much attention. The band gaps of SnO_2 and TiO_2 are 3.88 and 3.2 eV, respectively, and the conduction band of SnO_2 is approximately 0.5 V more positive than that of TiO_2 [27]. When the two semiconductor particles are coupled, the conduction band of SnO_2 acts as a sink for photogenerated electrons. Since the photogenerated holes move in the opposite direction, they accumulate in the valence band of the TiO_2 particle, thereby increasing the efficiency of charge separation [27, 28]. Two variants of SnO_2/TiO_2 system has been studied for the improvement of photoactivity i.e. composite SnO_2/TiO_2

†E-mail: andri.vital@empa.ch

particles/films [29–31] and mixed oxides of SnO_2/TiO_2 (substitution of Sn for Ti in TiO_2 lattice) [32]. Increase of the photoactivity with the mixed oxides is due to the increased band gap of the solid solution which necessitates the use of light of much higher energy (lower wavelengths). Sensato and co-workers [33] reported that increase in the band gap with the Sn content in the $Sn_xTi_{1-x}O_2$ system is in large part due to an increase in its conduction band. Since the conduction band shifts toward higher potential, the energy of the electrons on the conduction band have sufficient over-potential to efficiently reduce oxygen. Thus, the photoexcited electrons and holes in the $Sn_xTi_{1-x}O_2$ can be separated effectively and have a longer life time which increases the photocatalytic activity. On the other hand, theoretical band gaps of the SnO_2 and TiO_2 are preserved in the particles/films and due to this composite particles/films are interesting systems to study in more detail. Some authors reported the synthesis of SnO_2/TiO_2 particulate films and particles by using mixed suspensions of separate TiO_2, SnO_2 particles and calcining finally [29–31]. Shi and co-workers [34] reported the synthesis of SnO_2/TiO_2 coupled nanoparticles by homogenous solution precipitation method which includes multiple steps of adding $SnCl_4$ precursor to TiO_2 powder externally and subjecting the resultant powder to calcination. Resultant composite particles showed better photoactivity than pure ultrafine and commercial TiO_2 particles, and the optimum loading of SnO_2 on TiO_2 is reported as 18.4 wt%. Tai [35] reported the synthesis of particulate films by sol-gel method and maximum incident photon-to-current efficiency (IPCE) was obtained at an optimum film thickness of 3.5 and 7 μm for SnO_2 and TiO_2 respectively. By employing an optimum concentration [34, 35] of both species (SnO_2 and TiO_2) it is seen that better charge separation can be achieved to improve the efficiency of the photocatalytic process. However, coupled semiconductor particles prepared above were randomly distributed as they are prepared from a mixture of TiO_2 and SnO_2 colloidal solutions or of the colloidal SnO_2 with slurry of TiO_2 powder. Though Sn substitution enhances the transformation of anatase to rutile, Yang and co-workers [36] reported the synthesis of SnO_2/TiO_2 binary oxides by a novel stearic acid method (SAM) which stabilizes the anatase phase and showed better photocatalytic activity than P25. Above method is also a wet chemical synthesis route which needs calcination steps to improve the crystallinity of the resultant powder. Vemury and co-workers [37] synthesized the Sn doped TiO_2 nanoparticles by flame aerosol process, but didn't investigated the photocatalytic activity of the same.

In this paper we report the photocatalytic activity of the flame synthesized SnO_2/TiO_2 composite nanoparticles. Powders of high crystallinity have been produced which do not need any further calcination. Gas phase process employed in this study enables the mixing of the constituents at a molecular level to achieve better chemical homogeneity. To obtain this coupled nanoparticles, a stream of N_2 containing evaporated tetramethly tin (TMT) and titanium-tetraisopropoxide (TTIP) was brought into a methane-oxygen diffusion flame. Upon condensation, highly crystalline SnO_2/TiO_2 coupled nanoparticles were formed. In contrast to the equilibrium phase diagram of SnO_2/TiO_2, segregated phase of SnO_2 is observed. Composite particles are produced at various flow rates of oxidant and SnO_2 contents. Photocatalytic activity of the resultant particles is tested for decomposition of methylene blue and is found to vary with SnO_2 content.

2. EXPERIMENTAL PROCEDURE AND MATERIALS

2.1. Flame aerosol plant. Figure 1a shows the experimental set-up of the aerosol flame reactor schematically, the reactant dosing and delivery system and the particle collection unit. A co-flow diffusion burner consisting of three concentric tubes was used (Figure 1b).

Methane (CH_4, purity > 99.95%, Carbagas, Switzerland) was employed as fuel, and oxygen (O_2, purity > 99.95%, Carbagas, Switzerland) as oxidant. Titaniumtetraisopropoxide (TTIP, $Ti(C_3H_7O)_4$, purity > 99%, VWR International, Switzerland) and tetramethyl tin (TMT, $Sn(CH_3)_4$, purity > 99%, Fluka, Switzerland) were used as precursors for TiO_2 and SnO_2 respectively. Controlled amounts of precursors totalling 46 g/h were fed to the evaporator (Hovacal, IAS, Germany) through independent mass flow controllers (Bronkhorst HI-TEC, Netherlands) and 120 l/h of nitrogen (N_2, purity > 99.995%, Carbagas, Switzerland) was used as carrier gas to transport the vaporized precursor mixture to the central tube of the burner. Oxygen was fed through the outer annulus, nitrogen (33 l/h) as a lift gas (to lift the flame from the burner face) through the inner annulus and methane (120 l/h) through the centre tube, resulting in a single diffusion flame. Experiments were performed with oxygen flow rates of 720 to 1200 l/h. The flow rates of the precursors were varied to produce the precursor concentrations in the flame as given in Table 1. All gas flow rates were controlled by mass flow controllers (Bronkhorst HI-TEC, Netherlands). The evaporator, the gas delivery tubes to the burner and the burner itself were kept at 175°C to prevent condensation of precursor vapours. The product particles were collected on borosilicate glass fiber filters (Type GF50, Schleicher and Schuell, Germany) placed inside an open-faced, stainless steel filter holder connected to a vacuum pump (Trivac A-D16A, Leybold, Switzerland). The filter (150 mm diameter) was fixed 55 cm vertically above the tip of the burner in all experiments.

2.2. Photochemical reactor and reaction vessel. Details of photochemical reactor have been reported

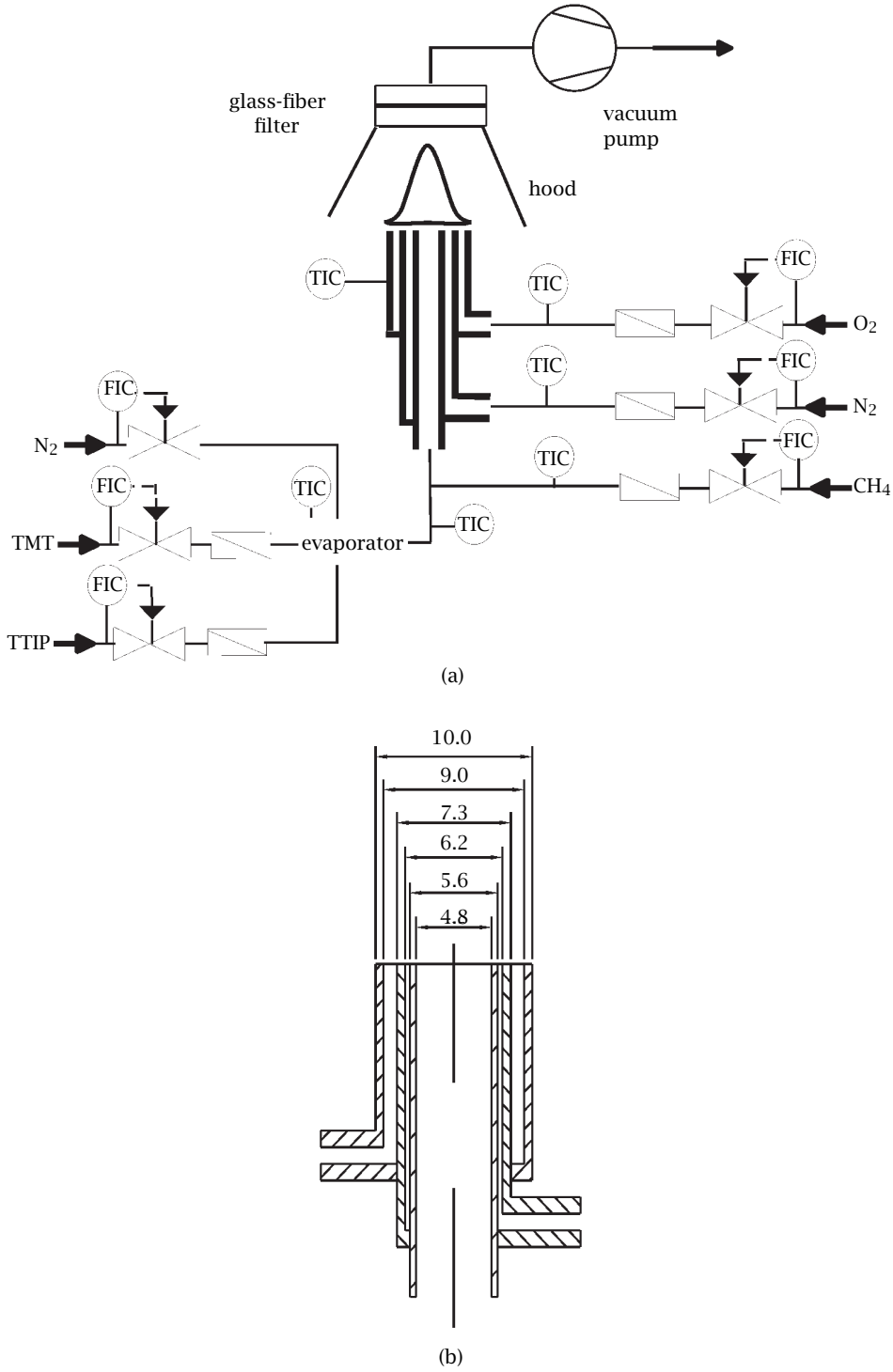

Figure 1. (a) *Experimental set-up for the synthesis of* SnO_2/TiO_2 *nanopowders by atmospheric pressure flame aerosol process;* (b) *cross section and tube dimensions (in* mm*) of the diffusion burner used.*

Table 1. *Vapour flow rates and resulting mole ratios of precursor species.*

Flow rate at STP (1/min)	TTIP	TMT	28.3 : 1 Ti : Sn	13.3 : 1 Ti : Sn	9 : 1 Ti : Sn	7 : 1 Ti : Sn	3.9 : 1 Ti : Sn
TTIP	0.0604		0.0591	0.0576	0.0564	0.0554	0.0533
TMT		0.0960	0.0020	0.0043	0.0062	0.0078	0.0112

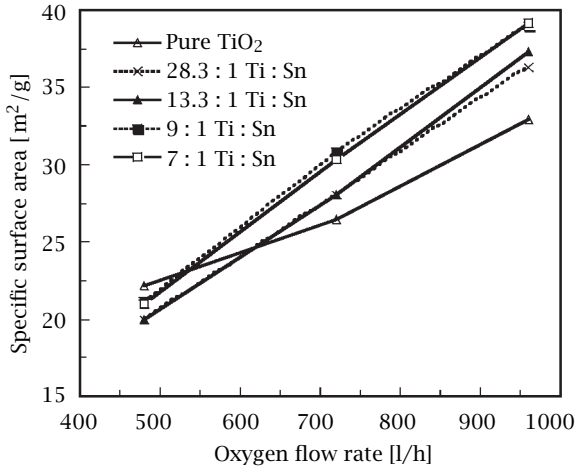

Figure 2. *Specific surface area of pure* TiO_2 *and* SnO_2/TiO_2 *composite powders synthesized as a function of oxygen flow rate and* Ti : Sn *ratio at* 120 l/h CH_4 *and* N_2.

elsewhere in detail [38, 39]. In brief, the photochemical reactor comprised two half-cylinders, each of which contained 6×8 W Coastwave Blacklight UVA lamps (Coast-AirR®; radiation λ (max.) = 355–360 nm; length = 28.7 cm) set against a half-cylinder aluminium reflector. The reaction vessel comprised a 125 cm^3 quartz Dreschel bottle fitted with a rubber septum, to allow samples from the reaction solution to be withdrawn online. Thermostatted water (30°C) was pumped continuously through the outer jacket of the reaction vessel.

A typical reaction solution placed in the photochemical reaction vessel comprised of 5.35×10^{-5} mol l^{-1} MB (methylene blue (≥ 82%), Acros Organics) dissolved in 125 cm^3 of deionized water containing 50 mg of photocatalyst. Degradation experiments were carried out at 303 K and at neutral pH. The reaction solution was continuously purged with air (160 ml/min) and magnetically stirred (300 rpm) throughout irradiation. Samples of the reaction solution were taken regularly as a function of time for the determination of MB concentration to follow its kinetics of disappearance by UV-Vis spectroscopy.

3. CHARACTERIZATION OF PHOTOCATALYST

The specific surface area (SSA) of the product powder was determined from a five point N_2 adsorption isotherm obtained from BET (Brunauer-Emmett-Teller) measurements using a Beckman-Coulter SA3100 (Beckman-Coulter, Switzerland). Prior to BET analysis, the powder samples were degassed at 200°C for 180 min under flowing N_2 atmosphere to remove adsorbed H_2O from the surface.

The primary particle size, shape and morphology of the particles were investigated by transmission electron microscopy (TEM). Powder samples were dispersed in isopropanol (purity > 99.5%, Fluka, Switzerland) and a few drops of the dispersion were allowed to dry on carbon-coated copper grids (Plano GmbH, Germany). The TEM analysis was performed on a Philips CM30 electron microscope operating at 200 kV. EDAX (Energy Dispersive X-ray Analysis) was performed using a Noran explorer X-ray detector, allowing the cross checking of chemical analysis of the particles.

X-ray diffraction (XRD) was used for identification of the crystal phases and determination of the average crystallite size. Diffraction measurements were performed with a PANalytical PW 3040/60 X'Pert PRO instrument using Ni-filtered Cu-Kα radiation of wavelength 1.5418 A°. A 2θ scan range from 5 to 80°, a scanning step size of 0.01° and a scintillation counter detector was used. Curve fitting and integration was carried out using proprietary software from Philips X'Pert high score plus.

Samples for UV-Vis spectroscopy were filtered through 0.2 μm Whatman Anotop 10 membrane filters to remove the catalyst particles before analysis. A Beer-Lambert diagram was established to correlate the absorbance at 660 nm to MB concentration.

4. RESULTS AND DISCUSSION

4.1. Catalyst characterization: BET, TEM and XRD. Figure 2 shows the specific surface area of the mixed SnO_2/TiO_2 aerosols at various concentrations of SnO_2 and as a function of oxygen flow rate. Increasing oxygen flow rate reduces the flame temperature [40] as additional O_2 flow dissipates the generated heat very quickly and shortens the flame length [41] as the combustion rate is enhanced [42]. Consequently, particle residence time at high temperatures is reduced and less growth species are generated by precursor oxidation [43]. Furthermore, the additional O_2 greatly dilutes the aerosol, and reduces the particle number concentration. Therefore, the collision rate of newly formed SnO_2/TiO_2 particles as well as the effective sintering time decreases, and this favours the formation and

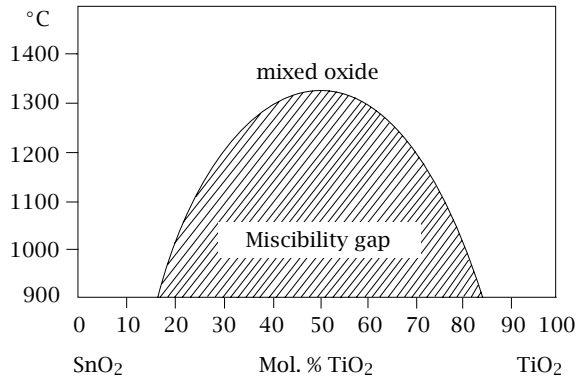

Figure 3. *Phase diagram of the* SnO_2/TiO_2 *system, adapted and modified from Padurow and co-workers* [49].

retention of small primary particles resulting in powders with high specific surface area. In contrast, the surface area of the mixed SnO_2/TiO_2 powders do not show much variation compared to the pure TiO_2. SnO_2 forms as a segregated phase within the TiO_2 particle (up to Ti : Sn of 13.3 : 1) though there is a complete solubility of one oxide in another in the solid phase (Figure 3). Because of the above reason, presence of SnO_2 didn't contribute to any significant changes in the surface area. Vemury and co-workers [37] synthesized the Sn doped TiO_2 and draw the same conclusion that the presence of SnO_2 does not affect the primary particle size or the surface area of the TiO_2 particles. Presence of SnO_2 as distinct primary particles is not seen until its concentration exceeds 13.3 : 1 mole ratio of Ti : Sn (Figures 4b and 4c). This is confirmed by the TEM pictures (Figure 5a) as the SnO_2 particles can be easily distinguished from TiO_2 because of its faceted morphology when compared to the spherical form of later (Figure 5b). Several authors reported that this difference in morphology stems from the difference in the particle formation and sintering mechanism. SnO_2 has a low melting point (1625°C) and sinters by evaporation-condensation mechanism [40], while titania sinters by grain boundary diffusion [44].

Figure 6 shows X-ray diffraction patterns of the mixed SnO_2/TiO_2 aerosols at various concentrations of SnO_2. In the 28.3 : 1 Ti : Sn sample neither reflections corresponding to cassiterite phase characteristic of segregated SnO_2 nor a shift of rutile reflection towards lower 2θ angle (characteristic of increased lattice parameter due to the solid solution of SnO_2 and TiO_2 [32]) is observed. For 13.3 : 1 Ti : Sn sample, reflections corresponding to segregated SnO_2 phase is observed and is confirmed by TEM and EDAX analysis that SnO_2 segregates within the TiO_2 particle. From 9 : 1 Ti : Sn samples, SnO_2 forms as distinct primary particles along with segregation within the TiO_2 particles (Figures 4b and 4c).

Addition of dopants is an effective way of controlling the phase composition of titania particles. Akhtar and co-workers [45] showed that adding $SiCl_4$, $POCl_3$ and BCl_3 during $TiCl_4$ oxidation inhibits the transformation of anatase to rutile, while adding $SnCl_4$ [37] and $AlCl_3$ [46] results in a substitutional solid solution that enhances the transformation to rutile. Vemury and co-workers [37] also synthesized SnO_2 doped TiO_2 particles in flame reactor and observed the decrease of intensity of anatase reflection even with the low concentration of SnO_2. In contrast, for the 28.3 : 1 of Ti : Sn sample, anatase phase is stabilized and its intensity increased consistent with the results obtained by Yang co-workers [36] during the synthesis of SnO_2/TiO_2 particles by stearic acid method. The ionic radius of Sn^{4+} is 0.69Å and is likely to substitute for Ti^{4+} (with an ionic radius of 0.61Å) in the titania lattice. Further, tin is in octahedral coordination with oxygen, with lattice parameters very close to those of rutile titania, (for SnO_2, $a = 0.4737$ nm and $c = 0.3186$ nm; for rutile TiO_2, $a = 0.4539$ nm and $c = 0.2958$ nm). The reason for this stabilization of anatase phase in 28.3 : 1 Ti : Sn sample is not understood well though Sn is reported as rutile stabilizer. The results obtained here cannot be directly compared with Vemury and co-workers [37] as they used different sources of precursors for SnO_2 and TiO_2 which can affect the particle nucleation and growth mechanism [47].

SnO_2 forms as segregated phase within the TiO_2 particle in 13.3 : 1 Ti to Sn sample. Dissolution of SnO_2 in TiO_2 is ruled out as there is no change in the lattice parameter of the later. Change of lattice parameter of $Sn_xTi_{1-x}O_2$ is systematically studied by Sensato and co-workers [33] and reported that lattice parameters vary non-linearly with composition supporting positive deviations from Vegard's law. Segregation of SnO_2 phase within the TiO_2 particle is seen by the atomic number contrast in the TEM images (Figure 4) [48]. The orientation of the crystalline region with respect to the electron beam (scattering contrast of TiO_2) may also affect contrast which can be falsely interpreted as the segregated SnO_2. In addition, if two particles are overlapping, the overlapped area will appear darker than the reminder of the particles. To cross check the contrast as segregated SnO_2, EDAX analysis was performed and confirmed that individual TiO_2 particles contain Sn as the other constituent. As the TEM pictures didn't show any separate SnO_2 particles (Figure 4a), and XRD pattern didn't show any shift of rutile peak towards lower 2θ angle (characteristic of solid solution of SnO_2/TiO_2) (Figure 6), this Sn signals should only come from segregated SnO_2 phase within the TiO_2 particle.

Examination of the equilibrium phase diagram (Figure 3) of SnO_2/TiO_2 [49] shows that the two oxides exhibit solid solubility at all compositions provided the processing temperature is more than 1300°C. As the temperatures of the flame reactors exceeds well above

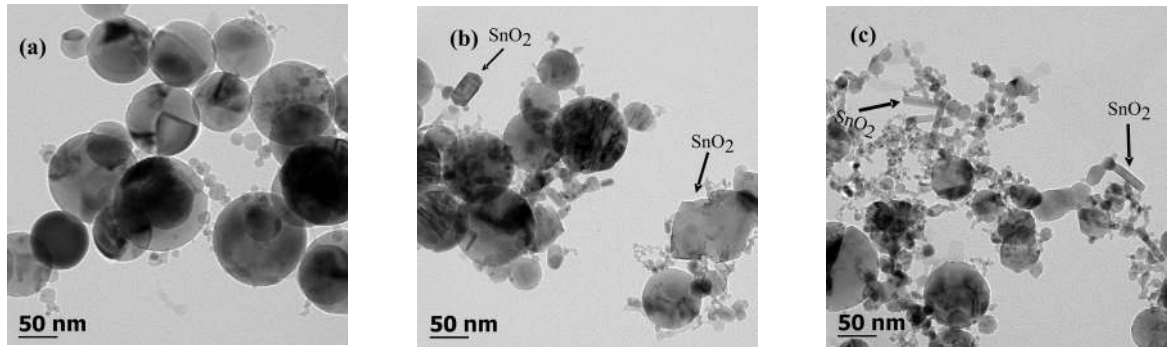

Figure 4. TEM *images of* SnO_2/TiO_2 *nanocomposites produced at various mole concentrations of* TMT/TTIP *precursors:* (a) Ti : Sn *ratio* 28.3 : 1, (b) Ti : Sn *ratio* 9 : 1 *and* (c) Ti : Sn *ratio* 7 : 1.

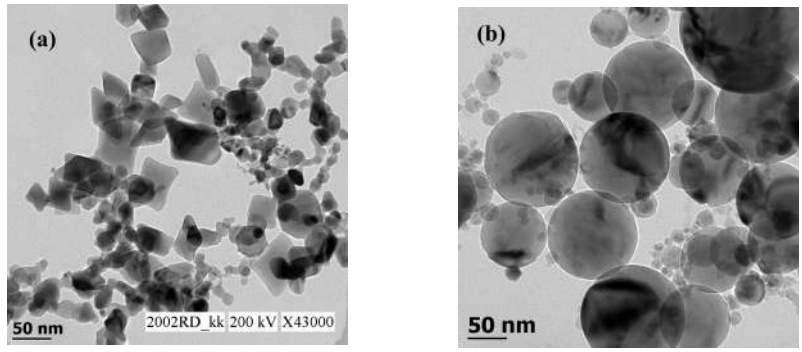

Figure 5. TEM *images of pure oxide particles synthesized at flow rates of* 480 l/h O_2, 120 l/h CH_4 *and* N_2*:* (a) SnO_2 *and* (b) TiO_2.

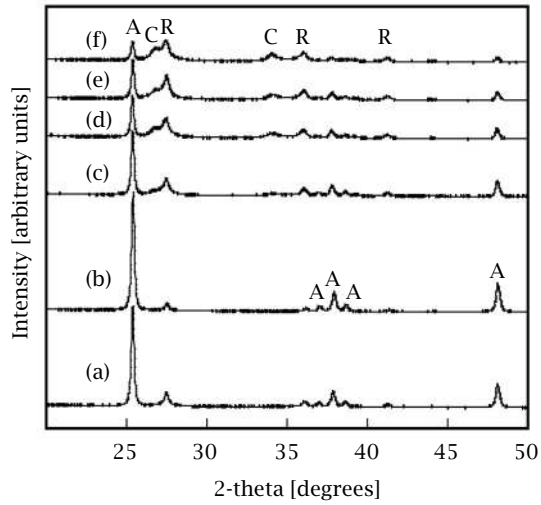

Figure 6. XRD *patterns of pure* TiO_2 *and* SnO_2/TiO_2 *powders produced at* 480 l/h O_2, 120 l/h CH_4 *and* N_2 *and at various concentrations of* TMT/TTIP*;* (a) *Pure* TiO_2, (b) 28.3 : 1 Ti : Sn, (c) 13.3 : 1 Ti : Sn, (d) 9 : 1 Ti : Sn, (e) 7 : 1 Ti : Sn *and* (f) 3.9 : 1 Ti : Sn*;* A-TiO_2 *anatase phase,* R-TiO_2 *rutile phase and* C-SnO_2 *cassiterite phase.*

1300°C [41], it is expected that SnO_2 and TiO_2 will form solid solutions at all compositions. Presence of segregated SnO_2 phase is related to the usage of diffusion flame instead of a premixed type. Premixed flame is characterized by a very different time-temperature history than the diffusion flame used in the present

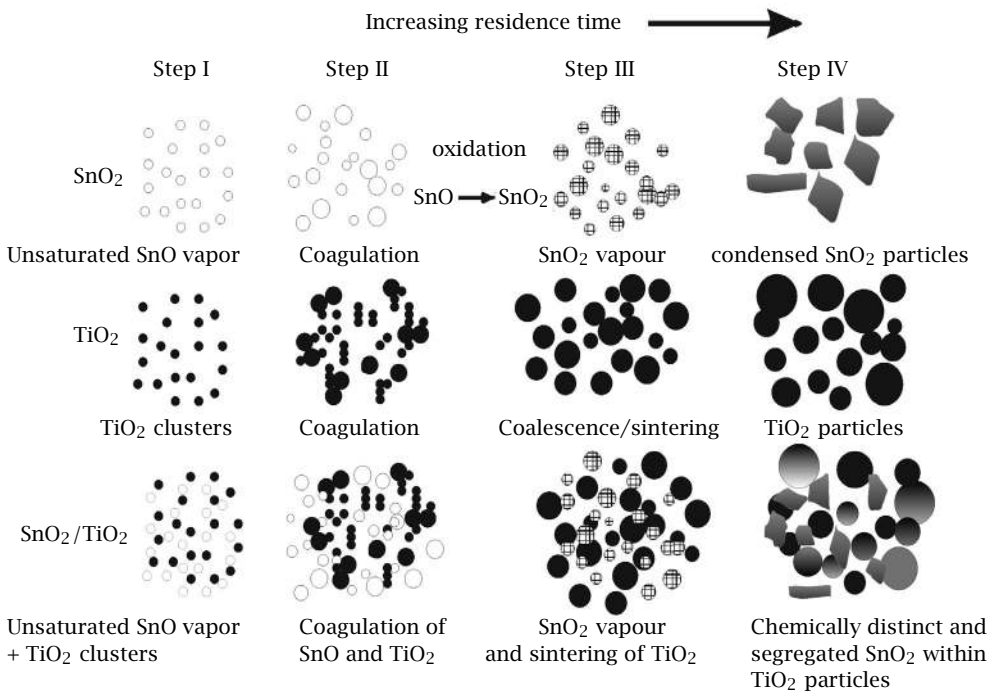

Figure 7. *Scheme of the particle growth processes for* SnO_2, TiO_2 *and* SnO_2/TiO_2 *composite particles.*

study [47]. The reaction zone of the premixed flame is characterized by high concentrations of radical species such as O, OH and H. As a result, precursor decomposition chemistry is driven by low activation energy radical abstraction reactions. Because of the fast radical driven decomposition of precursors, it is reasonable to expect that there will be little difference between precursor reaction rates i.e. both the precursors will decompose at the same time, in which case particles of uniform interparticle composition are formed. In contrast, for the diffusion flame, precursor decomposition chemistry is governed by thermal decomposition reactions. In addition, in the precursor decomposition/particle formation region of the burner, temperature increases with increasing residence time which means that the precursor with lowest activation energy for decomposition reacts first and chemical segregation/chemically distinct primary particles are expected to form [47]. TMT has low activation energy [50] for decomposition compared to TTIP [47] and due to this segregation of SnO_2 phase is seen within the TiO_2 particle at low mole ratios of Ti : Sn and chemically distinct SnO_2 primary particles at high mole ratios. Further more residence time of the particles in the flame is only few ms which may not facilitate to reach the equilibrium.

The processes occurring during multicomponent aerosol formation from the gas-phase precursors are the same as for the single component aerosol formation: Chemical reaction, nucleation and aerosol growth. Particle formation mechanism of individual SnO_2 [51] and TiO_2 [44] is reported by several authors. Basing on that we propose a mechanism for the SnO_2/TiO_2 system and is shown in (Figure 7). Initially, the TMT precursor is oxidized to form SnO vapor as the activation energy for decomposition of TMT is low. When TiO_2 particles start to nucleate, they form within the precursor vapour of SnO which subsequently oxidizes and condenses onto the existing TiO_2 particles (step III). SnO_2 condensed TiO_2 particles start to grow and retains the segregated phase. With increased concentration of TMT precursor in the mixed aerosol, SnO_2 forms as distinct primary particles along with the segregation within the TiO_2 particles (Figures 4b and 4c).

4.2. Photocatalytic degradation of MB. Photocatalytic activity of the pure TiO_2 and SnO_2/TiO_2 nanocomposites synthesized under similar conditions (7201/h O_2 flow rate) are tested for the degradation of MB after checking that there is no degradation with TiO_2 (no irradiation) or UV irradiation alone (no photocatalyst). Figure 8 shows the kinetics of disappearance of MB for pure TiO_2 and SnO_2/TiO_2 powder. It can be seen from the figure that SnO_2/TiO_2 composites (up to 7 : 1 Ti : Sn) shows better activity compared to pure TiO_2. In slurry based photocatalytic reactor systems, the rate-determining step in the degradation process is considered to be the reduction of oxygen (which is circulated in the reactor vessel) by the conduction band electrons [52]. Excited conduction band electrons must be separated spatially from the holes, because the

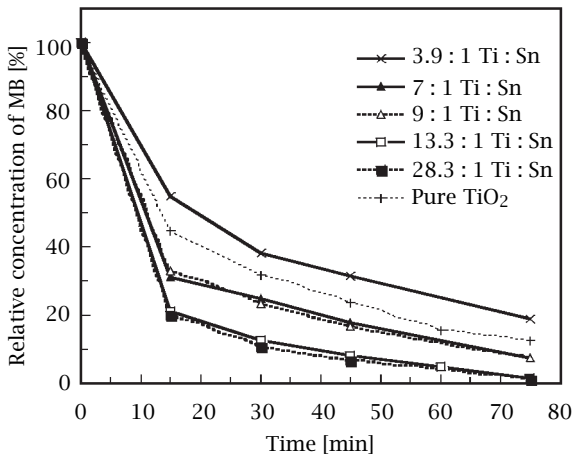

Figure 8. *Degradation profile of* MB *for pure* TiO_2 *and* SnO_2/TiO_2 *composite particles.*

characteristic time required for reduction ($\sim \mu$s) is generally much greater than that for oxidation ($\sim$ 100 ns) [53]. The potential of the conduction band electrons should be high in order to get scavenged by the oxygen and unless otherwise will recombine with the valence band hole. The potential of the conduction band is more negative for anatase compared to rutile and due to this anatase is considered as more beneficial for photocatalytic activity [54]. In the 28.3 : 1 Ti to Sn sample, anatase phase is stabilized and its intensity of reflection increased compared to pure TiO_2. This might be the reason for the increased photocatalytic activity of the sample mentioned above.

Alternatively photogenerated electrons can be separated from holes by coupling TiO_2 with SnO_2. Gerischer and co-workers [55] proposed a model regarding the role of oxygen in photo-oxidation of organic molecules which states that a sufficiently fast O_2 reduction rate for attaining high quantum efficiency is achieved only when catalytic sites are incorporated on the TiO_2 surface and is supported by several researches [13–17]. The 13.3 : 1 Ti to Sn sample showed similar activity like the 28.3 : 1 Ti to Sn sample for the MB decomposition, even though addition of SnO_2 extensively decreased the X-ray intensity of anatase phase. Increased photocatalytic activity of the 13.3 : 1 Ti to Sn sample is correlated to the segregated SnO_2 which acts as electron scavenger. The conduction band (CB) edges of TiO_2 and SnO_2 are situated at -0.34 and $+0.07$ eV versus normal hydrogen electrode (NHE) at pH 7, respectively. The valence band (VB) edge of SnO_2 ($+3.67$ eV) is much lower than that of TiO_2 ($+2.87$ eV) [56]. In terms of the energetics, electrons flow into the SnO_2, while holes oppositely diffuse into the TiO_2. Consequently, more holes reach the TiO_2 surface to cause oxidation reaction, whereas electrons withdrawing from the surface are probably consumed for reduction of O_2 at the edge of the segregated SnO_2. Thus the interfacial electron transfer from TiO_2 to SnO_2 can explain the higher photocatalytic activity of the composite particles.

Photocatalytic activity of the composites starts to decrease from 9 : 1 and 7 : 1 Ti : Sn samples but still better than the activity of pure TiO_2. The 3.9 : 1 Ti to Sn sample shows further decrease in activity and is inferior compared to pure TiO_2. Increasing the SnO_2 content means that there is a decrease in the active photocatalyst (TiO_2) content, as the former shows poor activity to decompose MB. So, 7 : 1 Ti to Sn (21 wt% SnO_2) sample is the maximum SnO_2 content up to which composites show better activity than pure TiO_2. Shi and coworkers [34] reported in the study of SnO_2-TiO_2 coupled particles that an optimum loading of 18.4 wt% SnO_2 is essential for improving the photoactivity, which agrees well with the results we got.

5. CONCLUSION

Formation of SnO_2/TiO_2 composite nanoparticles in atmospheric pressure diffusion flames has been investigated. Usage of diffusion flame configuration has been shown to influence the formation of multicomponent aerosols and non-equilibrium phases, making flame aerosol process a unique and inexpensive route to synthesize wide spectrum of new materials. The photocatalytic activity of the composite particles is higher than the pure TiO_2 synthesized under similar conditions and the maximum content of the SnO_2 for increased activity is 21 wt%. Improved photocatalytic activity is due to the nanocomposite structure of the particles and as a result thereof the low recombination rate of photoexcited electrons and holes facilitated by coupling of TiO_2 with SnO_2.

ACKNOWLEDGMENTS

The authors would like to acknowledge the EC and the Swiss BBW for their support of the FP5-Project Photocoat (EU contract No G5RD-CT-2002-00861; BBW project No 01.0571-1) and also Dr. Christian Soltmann, Dr. Hartmut Wiggers and Mr. Pascal Ifeacho for their contributions to this work.

REFERENCES

[1] A. Fujishima and K. Honda, Nature **37** (1972), 238.
[2] (a) I. Bedja, S. Hotchandani, and P. V. Kamat, J. Phys. Chem. **98** (1994), 4133. (b) S. Ferrere, A. Zaban, and B. A. Gregg, J. Phys. Chem. B. **101** (1997), 4490.
[3] (a) G. Redmond, D. Fitzmaurice, and M. Graetzel, Chem. Mater. **6** (1994), 686. (b) H. Rensmo, K. Keis, H. Lindstroem, S. Soedergren, A. Solbrand, A. Hagfeldt, S. E. Lindquist, L. N. Wang, and M. Muhammed, J. Phys. Chem. B. **101** (1997), 2598. (c) T. N. Rao and L. J. Bahadur, J. Electrochem. Soc. **144** (1997), 179.

[4] K. Sayama, H. Sugihara, and H. Arakawa, Chem. Mater. **10** (1998), 3825.
[5] A. Turkovic and Z. Crnjak Orel, Sol. Energy Mater. Sol. Cells **45** (1997), 275.
[6] M. Y. El Zayat, A. O. Saed, and M. S. El-Dessouki, Int. J. Hydrogen Energy **23** (1998), 259.
[7] R. E. Stephens, B. Ke, and D. Trivich, J. Phys. Chem. **59** (1955), 966.
[8] J. J. Rowlette, Sol. Energy **7** (1963), 8.
[9] A. Sclafani, L. Palmisano, and E. Davi, J. Photochem. Photobiol. A: Chem. **56** (1991), 113.
[10] O. Legrini, E. Oliveros, and A. M. Braun, Chem. Rev. **93** (1993), 671.
[11] M. R. Hoffmann, S. T. Martin, W. Y. Choi, and D. W. Bahnemann, Chem. Rev. **95** (1995), 69.
[12] G. Riegel and J. R. Bolton, J. Phys. Chem. **99** (1995), 4215.
[13] A. Wood, M. Giersig, and P. Mulvaney, J. Phys. Chem. B. **105** (2001), 8810.
[14] M. Jakob, H. Levanon, and P. V. Kamat, Nano. Lett. **3** (2003), 353.
[15] V. Subramanian, E. E. Wolf, and P. V. Kamat, J. Am. Chem. Soc. **126** (2004), 4943.
[16] T. Hirakawa and P. V. Kamat, Langmuir **20** (2004), 5645.
[17] T. Johannessen and S. Koutsopoulos, J. Catal. **205** (2002), 404.
[18] K. Tennakone and J. Bandara, Appl. Catal. A Gen. **208** (2001), 335.
[19] K. Vinodgopal, I. Bedja, and P. V. Kamat, Chem. Mater. **8** (1996), 2180.
[20] Y. R. Do, W. Lee, K. Dwight, and A. Wold, J. Solid State Chem. **108** (1994), 198.
[21] X. Z. Li, F. B. Li, C. L. Yang, and W. K. Ge, J. Photochem. Photobiol. A Chem. **141** (2001), 209.
[22] B. Pal, M. Sharon, and G. Nogami, Mater. Chem. Phys. **59** (1999), 254.
[23] B. Pal, T. Hata, K. Goto, and G. Nogami, J. Mol. Catal. A Chem. **169** (2001), 147.
[24] C. Wang, J. C. Zhao, X. M. Wang, B. X. Mai, G. Y. Sheng, P. J. Peng, and J. M. Fu, Appl. Catal. B Environ. **39** (2002), 269.
[25] L. Spanhel, H. Weller, and A. Henglein, J. Am. Chem. Soc. **109** (1987), 6632.
[26] L. Spanhel, A. Henglein, and H. Weller, Ber. Bunsen-Ges. Phys. Chem. **91** (1987), 1359.
[27] U. Stafford, K. A. Gray, and P. V. Kamat, Chem. Rev. **3** (1996), 77.
[28] P. V. Kamat and K. Vinodgopal, *Organic and Inorganic Photochemistry*, Marcel Dekker, New York, 1998.
[29] J. Shang, W. Yao, Y. Zhu, and N. Wu, Appl. Catal. A: General **257** (2004), 25.
[30] N. Kanai, T. Nuida, K. Ueta, K. Hashimoto, T. Watanabe, and H. Ohsaki, Vacuum **74** (2004), 723.
[31] L. Cao, H. Wan, L. Huo, and S. Xi, J. Colloid. Inter. Sci. **244** (2001), 97.
[32] J. Lin, J. C. Yu, D. Lo, and S. K. Lam, J. Catal. **183** (1999), 368.
[33] F. R. Sensato, R. Custodio, E. Longo, A. Beltran, and J. Andres, Catal. Today **85** (2003), 145.
[34] L. Shi, C. Li, H. Gu, and D. Fang, Mat. Chem. Phys. **62** (2000), 62.
[35] W. P. Tai, Mater. Letters **51** (2001), 451.
[36] J. Yang, D. Li, X. Wang, X. Yang, and L. Lu, J. Solid. State. Chem. **165** (2002), 193.
[37] S. Vemury and S. E. Pratsinis, J. Am. Ceram. Soc. **78** (1995), 2984.
[38] A. Mills, S. Morris, and R. Davies, J. Photochem. Photobiol. A: Chem. **70** (1993), 183.
[39] A. Mills and S. Morris, J. Photochem. Photobiol. A: Chem. **71** (1993), 75.
[40] W. Zhu and S. E. Pratsinis, AICHE Journal. **43** (1997), 2657.
[41] R. Mueller, H. K. Kammler, S. E. Pratsinis, A. Vital, G. Beaucage, and P. Burtscher, Powder Technol. **140** (2004), 40.
[42] S. E. Pratsinis, W. Zhu, and S. Vemury, Powder Technol. **86** (1996), 87.
[43] W. Zhu and S. E. Pratsinis, Am. Chem. Soc. Symposium Series **622** (1996), 64.
[44] C. H. Hung and J. L. Katz, J. Mater. Res. **7** (1992), 1861.
[45] M. K. Akhtar, S. E. Pratsinis, and S. V. R. Mastrangelo, J. Am. Cerm. Soc. **75** (1992), 3408.
[46] M. K. Akhtar, S. E. Pratsinis, and S. V. R. Mastrangelo, J. Mater. Res. **9** (1994), 1241.
[47] S. H. Ehrmann, S. K. Friedlander, and M. R. Zachariah, J. Aerosol Sci. **29** (1998), 687.
[48] D. B. Williams and C. B. Carter, *Transmission Electron Microscopy III*, Plenum Press, New York, 1996.
[49] N. N. Padurow, Die Naturwissenschaften **43** (1956), 395.
[50] S. W. Lee and C. Yoon, Bull. Korean Chem. Soc. **20** (1999), 1031.
[51] K. K. Akurati, R. Dittmann, A. Vital, U. Klotz, P. Hug, T. Graule, and M. Winterer, Submitted to J. Nanoparticle Res. (2004).
[52] G. P. Fotou and S. Pratsinis, Chem. Eng. Commun. **251** (1996), 151.
[53] M. R. Hoffmann, S. T. Martin, W. Choi, and D. Bahnemann, Chem. Rev. **95** (1995), 69.
[54] D. F. Ollis, E. Pelizzetti, and N. Serpone, *Photocatalysis, Fundamentals and Applications*, John Wiley, New York, 1989, 603.
[55] H. Gerischer and A. Heller, J. Phys. Chem. **95** (1991), 5261.
[56] A. Hattori, Y. Tokihisa, H. Tada, and S. Ito, J. Electrochem. Soc. **147** (2000), 2279.